Characteristic, dynamic, and near-saturation regions of out-of-time-order correlation in Floquet Ising models

Rohit Kumar Shukla [*] and Sunil Kumar Mishra [†]

Department of Physics, Indian Institute of Technology (Banaras Hindu University), Varanasi 221005, India

We study characteristic, dynamic, and saturation regimes of the out-of-time-order correlation (OTOC) in the constant-field Floquet system with and without longitudinal field. In the calculation of OTOC, we take local spins in longitudinal and transverse directions as observables which are local and nonlocal in terms of Jordan-Wigner fermions, respectively. We use the exact analytical solution of OTOC for the integrable model (without the longitudinal field term) with transverse direction spins as observables and numerical solutions for other integrable and nonintegrable cases. OTOCs in both cases depart from unity at a kick equal to the separation between the observables when the local spins are in the transverse direction, and one additional kick is required when the local spins are in the longitudinal direction. The number of kicks required to depart from unity depends on the separation between the observables and is independent of the Floquet period and system size. In the dynamic region, OTOCs show power-law growth in both models, the integrable one (without longitudinal field) and the nonintegrable one (with longitudinal field). The exponent of the power-law increases with increasing separation between the observables. Near the saturation region, OTOCs grow linearly at a very low rate.

I. INTRODUCTION

Larkin and Ovchinnikov first introduced the concept of out-of-time-order correlation (OTOC) for defining approaches from quasiclassical to quantum systems [1]. In recent years OTOCs have gotten attention in various fields [2–10], such as quantum chaos and information propagation in quantum many-body systems [11–17], quantum entanglement and quantum information delocalization [6,18–23], and static and dynamical phase transitions [9,24,25]. Several ideas for experimental measurement of OTOCs were proposed [26–30] using cold atoms or cavity and circuit quantum electrodynamics (QED) or trapped-ion simulations. Experimental realizations were made using nuclear spins of molecules [19,25,31], trapped ions [32,33], and ultracold gases [34]. The chaotic characteristics of OTOC manifest if a small disturbance in the input of the system causes an exponential deviation in the output of the system, which is known as the butterfly effect [16,35].

Classical Hamiltonian systems which have the highest amount of randomness and chaos are converted into the quantum domain for observing the behavior of quantum chaos [4,5]. OTOC finds a role in characterizing the quantum chaos in these systems. A characteristic form of growth of OTOC exists that can distinguish different classes of information scrambling. In a chaotic case, OTOC grows very fast, which is often described by an exponential behavior with a Lyapunov exponent. If the chaos is absent, the growth of OTOC can be much slower or even absent. In disordered systems, OTOC distinguishes many-body localization [36–38] from the Anderson localization [39].

Growth of OTOC is also discussed in spin systems [20,40–50]. Power-law growth of OTOC is observed in the dynamic region of the Luttinger-liquid model [48], XY model [47], integrable quantum Ising chain [20], and some systems exhibiting many-body localization [49,50]. Similar studies have been done with the Ising model with tilted magnetic fields, perturbed XXZ model, and Heisenberg spin chain with random magnetic fields [43]. In these systems, OTOC is calculated for different types of observables. For the observables that are local, nonlocal, or mixed in terms of the Jordan-Wigner (JW) fermions, the OTOCs grow as a power law in time [20].

Quantum systems periodically driven by external forces have received considerable attention for a very long time. Examples are the kicked-rotor model, in which particles move on a ring and field is applied in the form of kicks [51]; the Chirikov standard map [52]; and the Kapitza pendulum [53]. These systems show the transition from integrability to chaos, dynamical localization [54,55], and dynamical stabilization [53,56]. In recent years, in quantum domains such as time crystals [57,58], the topological system with ultracold atoms [59,60], periodically driven quantum systems such as particles moving in a modulated harmonic trap [61], kicked quantum rotors [62–64], Floquet spin systems with constant fields [9,65–69], and quenched fields [70–74] have received considerable attention. Periodic perturbation can be realized in experiments to understand specific properties of matter [62,75–77]. OTOC generated by the sum of quadratic and composite observables in terms of Majorana fermions studied in integrable and nonintegrable kicked quantum Ising systems [42] shows linear growth with time and starts to saturate at $t \simeq$

---

*rohitkrshukla.rs.phy17@itbhu.ac.in
†sunilkm.app@iitbhu.ac.in

022403-1

$N/2$, where N is the system size. OTOCs using local and non-local observables for Floquet XY and synchronized Floquet XY models were also studied recently [78]. In our previous study [9], we were able to get the phase structure using time-averaged longitudinal magnetization OTOC (LMOTOC), but transverse magnetization OTOC (TMOTOC) failed to give us the phase diagram. While thoroughly understanding the comparison between the initial and time-averaged behaviors of integrable TMOTOC and LMOTOC, we found different characteristic times. In this paper, we carry out a comprehensive study of the entire region of OTOC in the integrable and nonintegrable Floquet spin models, not just the initial time or averaged behavior. We will analyze whether the integrability-breaking term changes the growth of OTOC. We extract the differences and similarities of TMOTOC and LMOTOC for integrable and nonintegrable models.

This paper is structured as follows: In Sec. II, we discuss the Floquet transverse Ising models. Subsequently, in Sec. III, we define TMOTOC and LMOTOC. Then, we discuss results in Sec. IV, while comparing the calculations of integrable and nonintegrable Floquet transverse Ising models in both TMOTOC and LMOTOC. Finally, we conclude the results in Sec. V.

II. MODEL

Consider a periodically driven interacting transverse Ising Floquet system. The Hamiltonian of the system is given as

$$\hat{H}(t) = J_x \hat{H}_{xx} + h_z \sum_{n=-\infty}^{\infty} \delta\left(n - \frac{t}{\tau}\right)\hat{H}_z, \quad (1)$$

where J_x is the nearest-neighbor exchange coupling strength and h_z is the external field in the transverse direction applied in the form of kicks at equal intervals of time τ. $\hat{H}_{xx} = \sum_{l=1}^{N} \hat{\sigma}_x^l \hat{\sigma}_x^{l+1}$ is the nearest-neighbor Ising interaction term, and $\hat{H}_z = \sum_{l=1}^{N} \hat{\sigma}_z^l$ is the interaction of unit magnetic field with the total transverse magnetization.

The Floquet map corresponding to Eq. (1) is

$$\hat{\mathcal{U}}_0 = \exp(-i\tau J_x \hat{H}_{xx}) \exp(-i\tau h_z \hat{H}_z) \quad (2)$$

In Eqs. (1) and (2) only transverse field is present and the Hamiltonian is exactly solvable using JW transformation [66,79,80]. Now, if we introduce a longitudinal field term $h_x \hat{H}_x = h_x \sum_{l=1}^{N} \hat{\sigma}_x^l$, the Hamiltonian can be written as

$$\hat{H}(t) = J_x \hat{H}_{xx} + h_x \hat{H}_x + h_z \sum_{n=-\infty}^{\infty} \delta\left(n - \frac{t}{\tau}\right)\hat{H}_z. \quad (3)$$

However, the model could not be transformed into free fermions using the JW transformation because the longitudinal field term when transformed into JW fermions gives an interacting fermionic term [79,80]. The Floquet map corresponding to this model is

$$\hat{\mathcal{U}}_x = \exp[-i\tau(J_x \hat{H}_{xx} + h_x \hat{H}_x)] \exp(-i\tau h_z \hat{H}_z). \quad (4)$$

Henceforth, in this paper, we denote the integrable transverse Ising Floquet model by $\hat{\mathcal{U}}_0$ and the nonintegrable transverse Ising Floquet model by $\hat{\mathcal{U}}_x$.

III. TMOTOC AND LMOTOC

Let us consider a pair of observables $\hat{W}^l$ and $\hat{V}^m$ at the lth and mth sites, respectively. OTOC of these observables is defined as

$$C^{l,m}(n) = -\frac{1}{2}\langle[\hat{W}^l(n), \hat{V}^m(0)]^\dagger[\hat{W}^l(n), \hat{V}^m(0)]\rangle. \quad (5)$$

Observables $\hat{W}^l$ and $\hat{V}^m$ are separated by distance $\Delta l = |l - m|$. Initially, at $n = 0$, both the observables commute with each other, i.e., $[\hat{W}^l(0), \hat{V}^m(0)] = 0$. As time increases, higher-order terms of the time evolution of $\hat{W}^l(0)$ given by the Baker-Campbell-Hausdorff formula fail to commute with $\hat{V}^m$, resulting in noncommutative $\hat{W}^l(n)$ and $\hat{V}^m$. By examining the noncommutativity of $\hat{V}^m$ at different positions, one can quantify to some degree how $\hat{W}^l(n)$ spread over the space. Here $\hat{W}^l(n)$ is $(\hat{\mathcal{U}}_{x/0}^\dagger)^n \hat{W}^l(0)(\hat{\mathcal{U}}_{x/0})^n$. If $\hat{W}^l$ and $\hat{V}^m$ are Hermitian and unitary, OTOC simplifies to the form

$$C^{l,m}(n) = 1 - \Re[F^{l,m}(n)], \quad (6)$$

where $\Re$ represents the real part, $F^{l,m}(n) = \langle\hat{W}^l(n)\hat{V}^m(0)\hat{W}^l(n)\hat{V}^m(0)\rangle$ and $\langle\cdot\rangle$ denotes the quantum-mechanical average over the initial state.

OTOC is calculated with either the trace over a maximally mixed state or a thermal ensemble. The trace can be replaced by employing Haar random states of 2^N dimensions to evaluate expectation values, that is, $\text{Tr}[\hat{W}^l(n)\hat{V}^m(0)\hat{W}^l(n)\hat{V}^m(0)]/2^N \approx \langle\Psi_R|\hat{W}^l(n)\hat{V}^m(0)\hat{W}^l(n)\hat{V}^m(0)|\Psi_R\rangle$, where $|\Psi_R\rangle$ is a random state. We replaced the random state by two fully polarized special initial states according to the observables and found that there is no remarkable differences in the characteristic, dynamic, and saturation regions of OTOC. We observed only one difference in the saturation region; there are comparatively small oscillations when we consider the random state. A detailed discussion is given in Appendix A. Moreover, the special initial states may help us to get the exact analytical formula, at least for integrable OTOC cases with transverse-direction spins as observables.

In this paper we consider $\hat{W}^l$ and $\hat{V}^m$ as local Pauli operators either in the longitudinal direction $\hat{\sigma}_x^{l,m}$ or in the transverse direction $\hat{\sigma}_z^{l,m}$. For the Pauli operators in the transverse direction as local observables, the OTOC, in this paper, is defined as transverse magnetization OTOC and is given as

$$C_z^{l,m}(n) = 1 - \Re[F_z^{l,m}(n)], \quad (7)$$

where $F_z^{l,m}(n) = \langle\phi_0|\hat{\sigma}_z^l(n)\hat{\sigma}_z^m(0)\hat{\sigma}_z^l(n)\hat{\sigma}_z^m(0)|\phi_0\rangle$. In the fermionic representation, $\hat{\sigma}_z^l$ can be written as $\hat{\sigma}_z^l = -(\prod_{j<l} A^j B^j)A^l$, where A^l and B^l are defined by fermionic creation ($c^{l\dagger}$) and annihilation (c^l) operators as $A^l = c^{l\dagger} + c^l$ and $B^l = c^{l\dagger} - c^l$ [81]. Since $\hat{\sigma}_z^l$ contains the string operator, it is known as the nonlocal operator in terms of the Jordan-Wigner fermion [20,81].

For calculation purposes we take the initial state as $|\phi_0\rangle = |\uparrow\uparrow\uparrow \cdots \uparrow\rangle$, where $|\uparrow\rangle$ is the eigenstate of $\hat{\sigma}_z$ with an eigenvalue of $+1$. If the observables are taken as Pauli operators in the longitudinal direction of the Ising axis (i.e., the z axis), then OTOC will be referred to as longitudinal magnetization

OTOC. LMOTOC is given as

$$C_x^{l,m}(n) = 1 - \Re[F_x^{l,m}(n)], \qquad (8)$$

where $F_x^{l,m}(n) = \langle\psi_0|\hat{\sigma}_x^l(n)\hat{\sigma}_x^m\hat{\sigma}_x^l(n)\hat{\sigma}_x^m|\psi_0\rangle$. In the fermionic representation, $\hat{\sigma}_x^{l/m}$ can be written as $\hat{\sigma}_x^{l/m} = A^{l/m}B^{l/m}$. In the fermionic representation $\hat{\sigma}_x^{l/m}$ is known as the local observable [20,81]. In this case the initial state will be taken as $|\psi_0\rangle = |\rightarrow\rightarrow\rightarrow\cdots\rightarrow\rangle$, where $|\rightarrow\rangle$ is the eigenstate of $\hat{\sigma}_x$ with an eigenvalue of $+1$.

The analytical solution of TMOTOC for the initial state $|\phi_0\rangle = |\uparrow\uparrow\uparrow\cdots\uparrow\rangle$ and Floquet map defined by Eq. (2) with $J_x = 1$ and $h_z = 1$ was derived in Ref. [9] as

$$
\begin{aligned}
F_z^{l,m}(n) = 1 - \left(\frac{2}{N}\right)^3 \sum_{p,q,r} [&e^{i(p-q)(m-l)}|\Psi_r(n)|^2\Phi_p^*(n)\Phi_q(n) \\
&- e^{i(-r-q)(m-l)}\Psi_r(n)^*\Phi_p^*(n)\Phi_q(n)\Psi_{-p}(n) \\
&- e^{i(p+q)(m-l)}\Psi_q(n)\Psi_r(n)^*\Phi_p(n)^*\Phi_{-r}(n) \\
&+ e^{i(q-r)(m-l)}\Psi_q(n)\Psi_r(n)^*|\Phi_p(n)|^2],
\end{aligned} \qquad (9)
$$

where the expansion coefficients $\Phi_q(n)$ and $\Psi_q(n)$ are defined as

$$\Phi_q(n) = |\alpha_+(q)|^2 e^{-in\gamma_q} + |\alpha_-(q)|^2 e^{in\gamma_q}, \qquad (10)$$

$$\Psi_q(n) = \alpha_+(q)\beta_+(q)e^{-in\gamma_q} + \alpha_-(q)\beta_-(q)e^{in\gamma_q}. \qquad (11)$$

The phase angle γ_q and the coefficients $\alpha_\pm(q)$ and $\beta_\pm(q)$ are given by

$$\cos(\gamma_q) = \cos(2\tau)\cos(4\tau) - \cos(q)\sin(2\tau)\sin(2\tau), \qquad (12)$$

$$\alpha_\pm(q)^{-1} = \sqrt{1 + \left(\frac{\cos(2\tau) - \cos(\gamma_q \pm 2\tau)}{\sin(q)\sin(2\tau)\sin(2\tau)}\right)^2}, \qquad (13)$$

$$
\begin{aligned}
\beta_\pm(q) = &\frac{\mp\sin(\gamma_q) - \cos(2\tau)\sin(2\tau)[\cos(q)+1]}{\sin(q)\sin(2\tau)} \\
&\times \alpha_\pm(q)e^{-i2\tau}.
\end{aligned} \qquad (14)
$$

The allowed values of p, q, and r are from $\frac{-(N-1)\pi}{N}$ to $\frac{(N-1)\pi}{N}$, differing by $\frac{2\pi}{N}$ for an even number of N_F ($N_F = \sum_l c_l^\dagger c_l$, the number of fermions) and $\hbar = 1$. We use the above exact solution to calculate TMOTOC for the integrable $\hat{\mathcal{U}}_0$ model. However, TMOTOC for the nonintegrable $\hat{\mathcal{U}}_x$ model and LMOTOC for both the integrable $\hat{\mathcal{U}}_0$ and nonintegrable $\hat{\mathcal{U}}_x$ models will be calculated numerically.

IV. RESULTS

We analyze TMOTOC and LMOTOC for both the $\hat{\mathcal{U}}_0$ and $\hat{\mathcal{U}}_x$ models in the following three regions, as depicted in Fig. 1.

(i) *Characteristic region.* Both observables $\hat{W}^l$ and $\hat{V}^m$ commute with each other until the characteristic time $t_{\Delta l}$, which is defined as the time after which $C_{z/x}^{l,m}(n)$ [$F_{z/x}^{l,m}(n)$] deviates from 0 (1). The characteristic time depends upon the separation between the spins ($\Delta l = |l - m|$). As we increase the separation between the spins, the characteristic time increases, and it is independent of the Floquet period and system size.
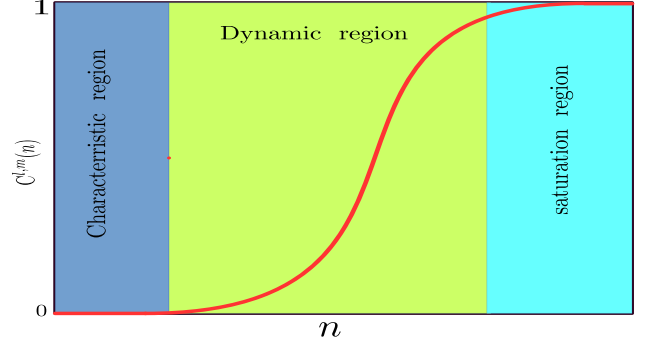

FIG. 1. Schematic of the various regions of OTOC in a typical system.

(ii) *Dynamic region.* After the characteristic time, $C_{z/x}^{l,m}(n)$ becomes nonzero. In this dynamic region $C_{z/x}^{l,m}(n)$ increases rapidly.

(iii) *Near-saturation region.* After rapid growth, $C_{z/x}^{l,m}(n)$ starts to saturate to a finite value. However, the manner in which $C_{z/x}^{l,m}(n)$ saturates follows some trend with an oscillating amplitude. We calculate such a trend by analyzing the behavior of $\Re[F_{z/x}^{l,m}(n)]$ vs n.

Let us begin with TMOTOC for the $\hat{\mathcal{U}}_0$ system defined by Eq. (2). First, we focus on the characteristic region of TMOTOC with an increasing Floquet period. Let us consider an operator $\hat{W}$ located at site l initially. We can see that the considered Floquet evolution increases the size of $\hat{W}$ at each Floquet step. In particular, the left end of the support of $\hat{W}(n)$ and the right end of the support of $\hat{W}(n)$ will increase by 1 for each Floquet step. We therefore can see that $F_z^{l,m}(n) = 1$ if $n < |l - m|$. However, once $n \geq |l - m|$, $F_z^{l,m}(n)$ will start to deviate from 1.

Figure 2(a) shows the behavior of $F_z^{l,m}(n)$ with an increasing Floquet period and fixed $\Delta l = 6$. We can see from Fig. 2(a) that $F_z^{l,m}(n)$ starts to deviate at the Δlth (= sixth) kick for the whole Floquet period τ. This characteristic time is independent of the Floquet period of the system size N (we have checked to $N = 50$). For a fixed Floquet period τ we can see the behavior of $\Re[F_z^{l,m}(n)]$ with the number of kicks and see the dependence of $t_{\Delta l}$ on Δl. In Fig. 2(b), for $\tau = \frac{6\epsilon}{2}$, we show $\Re[F_z^{l,m}(n)]$ vs the number of kicks by changing the separation between the observables $\Delta l = |l - m|$. We see that increasing the separation between the spins increases the characteristic time of the TMOTOC case and the number of kicks required to deviate from unity is equal to the separation between the observables ($n = \Delta l$). The growth of TMOTOC in the dynamic region follows a power law. The exponent of the power law increases with the increase in the separation between the local spin observables in a systematic manner [Fig. 2(c)]. The exponent increases, reaches maximum at $\Delta l = \frac{N}{2}$, and then decreases with increasing the distance between the spins [Fig. 2(d)]. The exponent of the power law can be expressed as a triangular function:

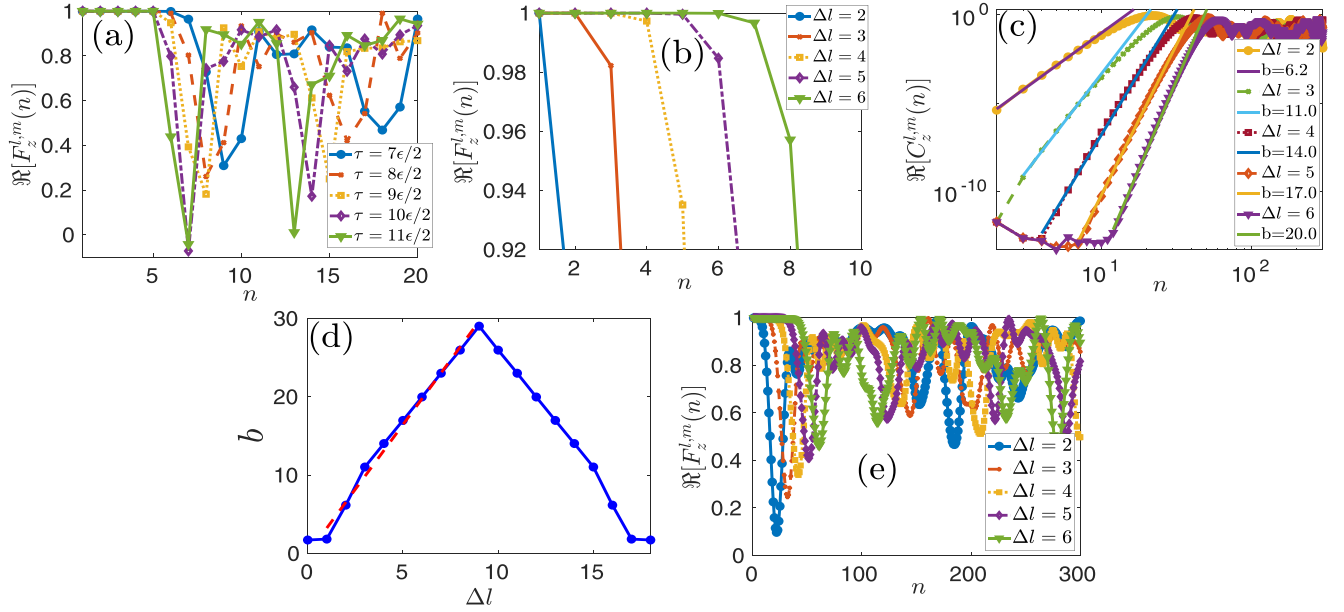$$b \approx b_{\max} - \kappa\left|\frac{N}{2} - \Delta l\right|, \qquad 1 \leq \Delta l \leq N-1, \quad (15)$$

FIG. 2. Integrable transverse Ising Floquet system with $J_x = 1$ and $h_z = 1$ for $N = 18$. (a) Behavior of TMOTOC with the number of kicks n while increasing the value of the Floquet period from $\frac{7\epsilon}{2}$ to $\frac{11\epsilon}{2}$ (right to left), differing by $\epsilon/2$, with fixed $\Delta l = 6$ ($\epsilon = \frac{\pi}{28}$). (b) $F_z^{l,m}$ with the number of kicks while increasing Δl (left to right) and fixed Floquet period $\tau = 6\epsilon/2$. (c) $C_z^{l,m}$ with the number of kicks (log-log) with increasing Δl (left to right) at constant Floquet period $\tau = \frac{\epsilon}{2}$. (d) Exponent of the power law with increasing distance between the spins. (e) $\Re[F_z^{l,m}]$ with the number of kicks at different increasing Δl (left to right).

where the constants $\kappa = 3.2$, $b_{\max} = 29$, and $b_0 = 1.7$. Equation (15) shows the dependence of the exponent of power law on increasing the separation between the observables. It is symmetric about $\Delta l = \frac{N}{2}$ because of the periodic boundary condition of the spin chains. $\Re[F_z^{l,m}(n)]$ reverts back to unity after a few kicks in the saturation region. Revival time has nontrivial dependence on n and Δl [Fig. 2(e)]. TMOTOC extracted from the analytical expression (9) in the characteristic, dynamic, and saturation regions can be summarized as

$$C_z^{l,m}(n) \approx \begin{cases} 0, & n\tau < t_{\Delta l}, \\ (n\tau)^{\kappa \Delta l + 2}, & t_{\Delta l} < n\tau < t_s, \\ \text{reverted back}, & t_s < n\tau. \end{cases} \quad (16)$$

In the above expression $t_{\Delta l}$ is the characteristic time, and t_s is the time at which TMOTOC starts saturating. The dynamic region of TMOTOC decreases with increasing the Floquet period τ, as shown in Figs. 3(a)–3(e). In general the dependence on τ is such that we can define $C_z^{l,m} \propto (n\tau)^{\kappa \Delta l + 2}$ in the dynamic region.

Now, we use the nonintegrable $\hat{\mathcal{U}}_x$ model given by Eq. (4) and analyze TMOTOC. Figure 4(a) shows the behavior of $F_z^{l,m}(n)$ for varying τ and fixed $\Delta l = 6$. From Fig. 4(a), we can see that the number of kicks required for $F_z^{l,m}(n)$ to deviate from unity is equal to the separation between the observables ($n = |l - m|$). Hence, the characteristic time does not depend on the Floquet periods. Let us explore the behavior of TMOTOC with distance between the spins for a fixed τ (say, $\tau = \frac{6\epsilon}{2}$) and increase the separation between the spins Δl. As Δl increases, the characteristic time $t_{\Delta l}$ increases in such a way that $n = \Delta l$ [Fig. 4(b)]. The dynamic region of TMOTOC for the nonintegrable model again shows a power-

law behavior, and the exponent of the power law b depends on Δl [Fig. 4(c)]. b increases with increasing Δl, reaches a maximum ($b_{\max}$) at $\Delta l = \frac{N}{2}$, and afterwards decreases symmetrically with increasing Δl before coming down to b_1 at $\Delta l = N - 1$. Since we consider the periodic boundary condition, the exponent of the power law is symmetric about $\Delta l = \frac{N}{2}$ [Fig. 4(d)]. In a mathematical form we can express b, approximately, by Eq. (15) with $\kappa = 3.2$, $b_{\max} = 28$, and $b_{\min} = 1.78$. Saturation of $\Re[F_z^{l,m}(n)]$ in this nonintegrable model follows a linear decaying behavior with a very small slope for all Δl [Fig. 4(e)]. TMOTOC for the $\hat{\mathcal{U}}_x$ model in all regions is summed up as

$$C_z^{l,m}(n) \approx \begin{cases} 0, & n\tau < t_{\Delta l}, \\ (n\tau)^{\kappa \Delta l + 1}, & t_{\Delta l} < n\tau < t_s, \\ 1 - \mu n, & t_s < n\tau, \end{cases} \quad (17)$$

where $\mu = 0.002$ and $\kappa = 3.2$. We calculate the exponent of the power law by using the Hausdorff-Baker-Campbell (HBC) formula for $\Delta l = 1, 2$ and find approximate matches with the exponent of the power law in the dynamic region of Eq. (17). The detailed calculation is given in Appendix B.

Now we focus on LMOTOC for the $\hat{\mathcal{U}}_0$ model, which shows similarity to TMOTOC for the same model. Figure 5(a) shows the behavior of LMOTOC at different Floquet periods and fixed $\Delta l = 6$. In LMOTOC, the number of kicks required to deviate from unity is $n = \Delta l + 1$. In comparison with TMOTOC, LMOTOC required one more kick to cause $F_x^{l,m}(n)$ to deviate from unity because $\hat{\sigma}_x^l$ (using the Baker-Campbell-Hausdorff formula) provide spreading terms after the first kick. Hence, the characteristic time does not depend on the Floquet period; however, it depends on the separation
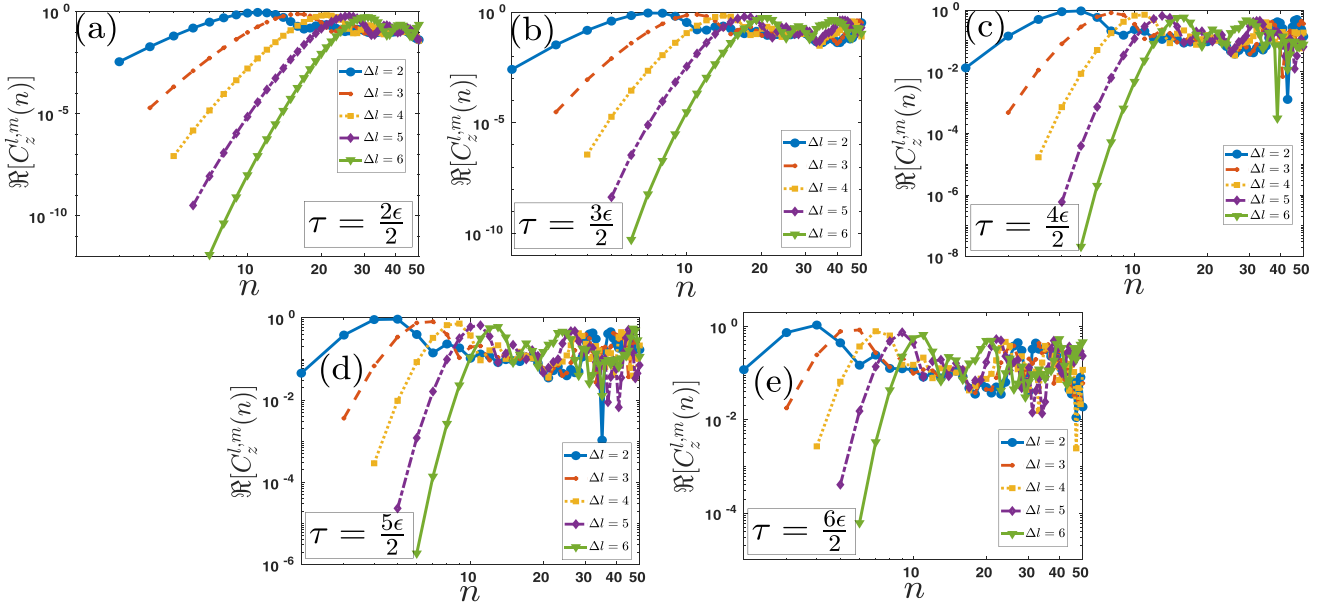
FIG. 3. Integrable transverse Ising Floquet system with $J_x = 1$ and $h_z = 1$ for $N = 18$. Behavior of TMOTOC with the number of kicks n while increasing Δl from 2 to 6 (left to right) at different Floquet periods: (a) $\tau = \frac{2\epsilon}{2}$, (b) $\tau = \frac{3\epsilon}{2}$, (c) $\tau = \frac{4\epsilon}{2}$, (d) $\tau = \frac{5\epsilon}{2}$, and (e) $\tau = \frac{6\epsilon}{2}$ ($\epsilon = \frac{\pi}{28}$).

between the observables in such a way that it increases linearly with increasing the separation between the observables ($n = \Delta l + 1$) [Fig. 5(b)]. In the dynamic region of LMOTOC with a small Floquet period, similar to the TMOTOC case, we get a power-law behavior. The exponent of the power law increases with Δl in the same manner as in the TMOTOC

case [Fig. 5(c)]. We can approximate the exponent with Δl by Eq. (15) with $\kappa = 3.4$, $b_{\max} = 32.9$, and $b_0 = 1.9$ [Fig. 5(d)]. The saturation region of LMOTOC for $\hat{\mathcal{U}}_0$ shows oscillating behavior. The envelope of the oscillation decays linearly with a constant slope for all Δl [Fig. 5(e)]. This behavior is in contrast to the saturation region of TMOTOC for $\hat{\mathcal{U}}_0$, which
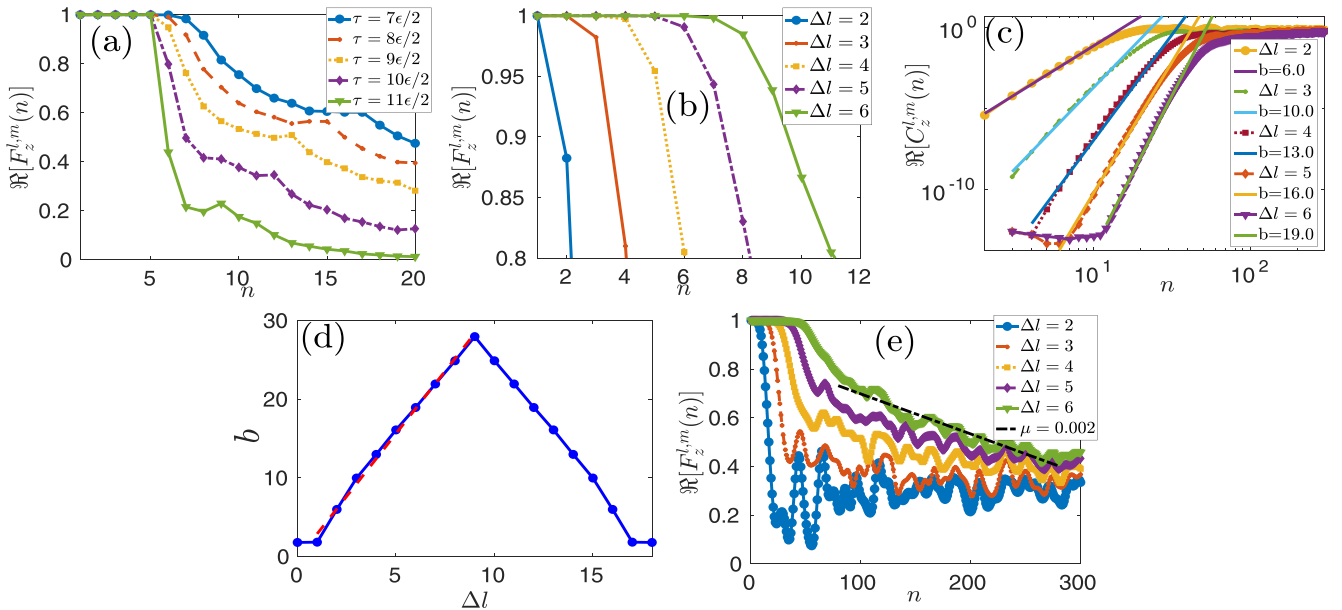

FIG. 4. Nonintegrable closed-chain transverse Ising Floquet system with $J_x = 1$, $h_z = 1$, and $h_x = 1$ of size $N = 18$. (a) Behavior of TMOTOC with the number of kicks n while increasing the value of the Floquet period from $\frac{7\epsilon}{2}$ to $\frac{11\epsilon}{2}$ (right to left), differing by $\frac{\epsilon}{2}$, with fixed $\Delta l = 6$ ($\epsilon = \frac{\pi}{28}$). (b) Initial region of $F_z^{l,m}$ with the number of kicks with increasing Δl (left to right) and fixed Floquet period $\tau = 6\epsilon/2$. (c) $C_z^{l,m}$ with the number of kicks (log-log) with increasing Δl (left to right) at fixed $\tau = \frac{\epsilon}{2}$. (d) Change in power with Δl. (e) Saturation of $F_z^{l,m}$ with the number of kicks at different increasing Δl (left to right). The black dash-dotted line represents the linear decrease of the maxima of the saturation amplitude.
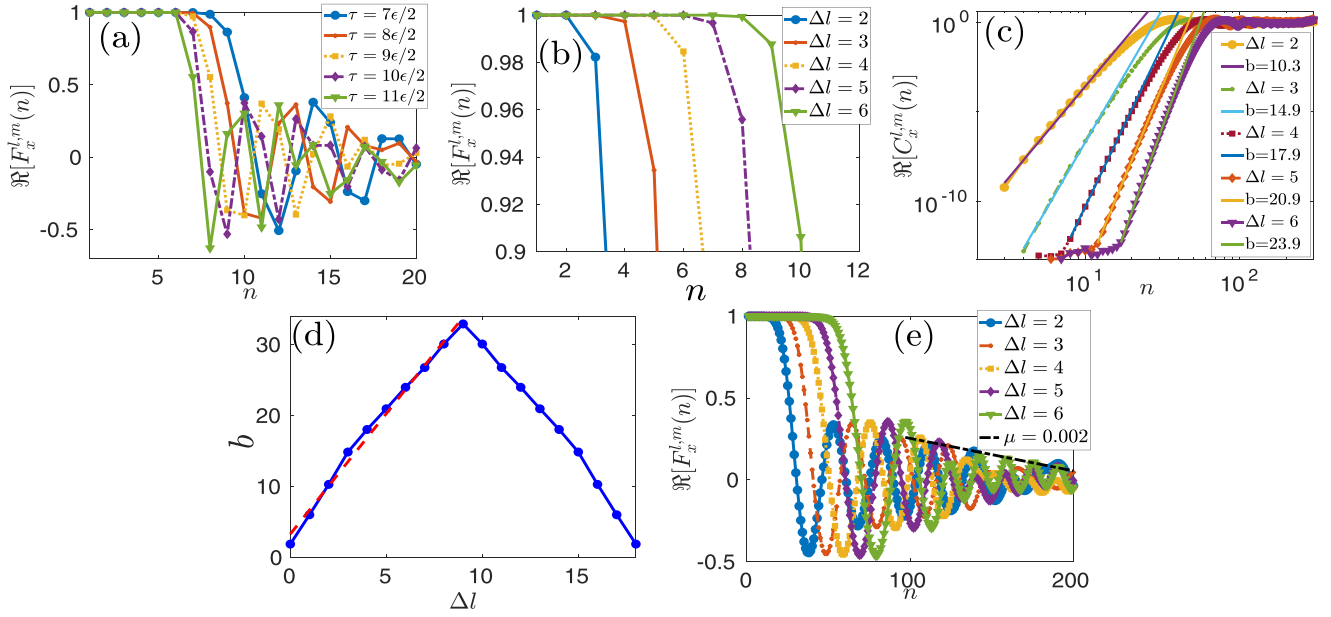
FIG. 5. Integrable closed-chain transverse Ising Floquet system with $J_x = 1$ and $h_z = 1$ of size $N = 18$. (a) Behavior of LMOTOC with the number of kicks n with increasing values of Floquet periods from $\frac{7\epsilon}{2}$ to $\frac{11\epsilon}{2}$ (right to left), differing by $\frac{\epsilon}{2}$, and $\Delta l = 6$ ($\epsilon = \frac{\pi}{28}$). (b) $F_x^{l,m}(n)$ with the number of kicks with increasing Δl (left to right) and fixed Floquet period $\tau = 6\epsilon/2$. (c) $C_x^{l,m}(n)$ with the number of kicks (log-log) with increasing Δl (left to right) at fixed $\frac{\epsilon}{2}$. (d) Change in power with Δl. (e) $F_x^{l,m}(n)$ with the number of kicks at different increasing Δl (left to right). The black dash-dotted line represents the linear decrease of the maxima of the saturation amplitude.

displays a reversal to early-time behavior. All the regions of LMOTOC for $\hat{\mathcal{U}}_0$ can be encapsulated as

$$C_x^{l,m}(n) \approx \begin{cases} 0, & n\tau < t_{\Delta l}, \\ (n\tau)^{\kappa\Delta l+6}, & t_{\Delta l} < n\tau < t_s, \\ 1 - \mu n, & t_s < n\tau. \end{cases} \quad (18)$$

Finally, we consider the $\hat{\mathcal{U}}_x$ model for LMOTOC calculations. We get a behavior in the characteristic regime similar to that for LMOTOC with the $\hat{\mathcal{U}}_0$ model [Figs. 6(a) and 6(b)]. In the dynamic region, the growth is again a power law, and the exponent increases with Δl [Fig. 6(c)], but the trend is a bit different than in the previous cases. Unlike in the previous cases, we see a quadratic increase of the exponent by increasing Δl, until a maximum is reached. After the maximum $b_{\max}$ at $\Delta l = \frac{N}{2}$, we see a symmetric decrease in the exponent until $\Delta l = N$ [Fig. 6(d)]. We approximate b as follows:

$$b \approx \left(b_{\max} - \lambda \left| \frac{N}{2} - \Delta l \right|^2 \right), \qquad 0 \leqslant \Delta l \leqslant N, \quad (19)$$

where $\lambda = 2.8$, $b_{\max} = 24.0$, and $b_0 = 1.7$. Equation (19) describes the variation of the exponent of the power law with increasing the separation between the observables. It is parabolic in form, with the vertex at $\frac{N}{2}$, and is also symmetric about $\Delta l = \frac{N}{2}$ because of the closed-chain consideration. We calculate the exponent of the power law by using the HBC formula for $\Delta l = 1$ and find that the exponent approximately matches Eq. (19). A detailed calculation is given in Appendix C. Saturation region of LMOTOC for the nonintegrable case is oscillating, and the maxima of the oscillation decreases linearly (with a very small slope $\mu = 10^{-5}$, which is the same for all Δl) with the number of kicks [Fig. 6(e)].

The total region of LMOTOC for the $\hat{\mathcal{U}}_x$ system is given as

$$C_x^{l,m}(n) \approx \begin{cases} 0, & n\tau < t_{\Delta l}, \\ (n\tau)^{\lambda(\Delta l)^2}, & t_{\Delta l} < n\tau < t_s, \\ 1 - \mu n, & t_s < n\tau. \end{cases} \quad (20)$$

In a nutshell, we see that the characteristic regions of LMOTOC have similar behavior for $\hat{\mathcal{U}}_0$ and $\hat{\mathcal{U}}_x$ systems. In both cases, the commutator propagation varies with τ in a similar way. But the dynamic region displays a contrast between $\hat{\mathcal{U}}_0$ and $\hat{\mathcal{U}}_x$. In the integrable case, the exponent of the power law increases linearly with Δl, but in the nonintegrable case, we see a quadratic growth of the power law with Δl. In the saturation region, both oscillate, and the envelope decreases at different rates.

In this paper we considered single spins as observables in our calculation of OTOCs. An experimental procedure for the calculation of OTOC using single-spin observables and the initial product state was given in Ref. [33]. Implementation of the unitary operator on observable $\hat{W}^l$ [$\hat{W}^l(n) = (\hat{\mathcal{U}}_x^\dagger)^n \hat{W}^l(0)(\hat{\mathcal{U}}_x)^n$] followed by perturbation of observable $\hat{V}^m$ was discussed in Ref. [82]. The OTOC is obtained by measuring the expectation value of the observable $(\hat{\mathcal{U}}_x^\dagger)^n \hat{W}^l(0)(\hat{\mathcal{U}}_x)^n \hat{V}^m (\hat{\mathcal{U}}_x^\dagger)^n \hat{W}^l(0)(\hat{\mathcal{U}}_x)^n \hat{V}^m$ [33]. Therefore, LMOTOCs and TOMOTOCs can be calculated experimentally.

V. CONCLUSION

We studied the behavior of TMOTOC and LMOTOC comprehensively using $\hat{\mathcal{U}}_0$ and $\hat{\mathcal{U}}_x$ systems. We divided LMOTOC and TMOTOC into three distinct regimes: the characteristic-
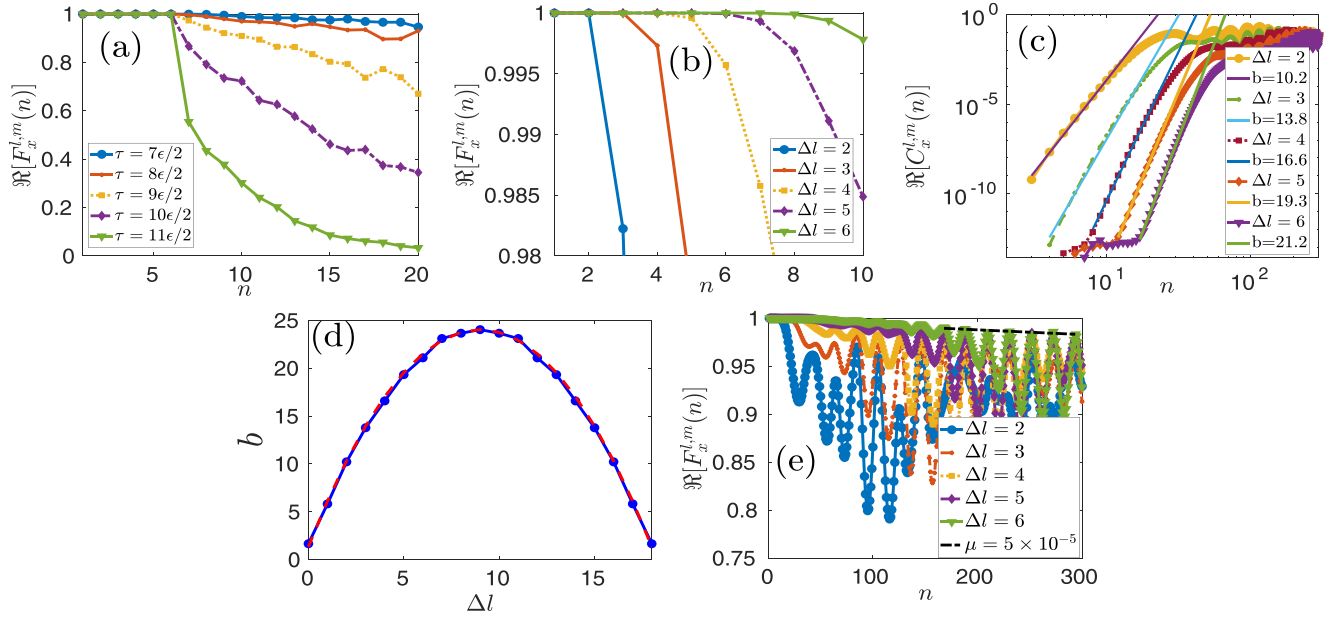
FIG. 6. Nonintegrable closed-chain transverse Ising Floquet system with $J_x = 1$, $h_z = 1$, and $h_x = 1$ for $N = 18$. (a) LMOTOC with the number of kicks n while increasing the value of the Floquet period from $\frac{7\epsilon}{2}$ to $\frac{11\epsilon}{2}$ (right to left) differing by $\frac{\epsilon}{2}$, with fixed $\Delta l = 6$ ($\epsilon = \frac{\pi}{28}$). (b) $F_x^{l,m}(n)$ with increasing Δl from 2 to 6 (left to right) and fixed period $\tau = \frac{6\epsilon}{2}$. (c) $C_x^{l,m}(n)$ with the number of kicks (log-log) while increasing Δl from 2 to 6 (left to right) and with fixed Floquet period $\tau = \frac{\epsilon}{2}$. (d) Change in power with Δl. (e) $F_x^{l,m}(n)$ with the number of kicks at different increasing Δl (left to right). The black dash-dotted line represents the linear decrease of the maxima of the saturation amplitude.

time regime, dynamic-time regime, and saturation-time regime.

Characteristic times of TMOTOC and LMOTOC are independent of the integrability of the system. They are also independent of the Floquet period and system size; however, they depend on the separation between the observables. The number of kicks required for $F^{l,m}$ to deviate from unity is equal to the numerical value of the separation between the observables in the case of TMOTOC; however, one extra kick is required in the case of LMOTOC. The behavior of the dynamic region is also independent of the integrability of the system. In both systems $\hat{\mathcal{U}}_0$ and $\hat{\mathcal{U}}_x$, LMOTOC and TMOTOC show power-law growth. There is no signature of the Lyapunov exponent. This power-law growth depends on

the separation between the spins and the Floquet period. The rate of change of the exponent with respect to the separation between the spins is independent of the integrability of the system in TMOTOC; however, we see a dependence in the case of LMOTOC. In TMOTOC for both systems $\hat{\mathcal{U}}_0$ and $\hat{\mathcal{U}}_x$, the exponent varies as a triangular function. In the case of LMOTOC, we see a triangular function with linear increase and decrease for the $\hat{\mathcal{U}}_0$ system but a quadratic increase and decrease for the $\hat{\mathcal{U}}_x$ system. The saturation region of TMOTOC is different in both systems: the $\hat{\mathcal{U}}_0$ system reverts back, but the $\hat{\mathcal{U}}_x$ system decays linearly. The saturation behavior of LMOTOC shows oscillating decay with the envelope decaying linearly in both systems. Saturation of TMOTOC and LMOTOC is independent of Δl.

APPENDIX A: CALCULATION OF TMOTOC IN THE NONINTEGRABLE $\hat{\mathcal{U}}_x$ SYSTEM USING THE RANDOM STATE

If $\hat{V}$ and $\hat{W}$ are two Hermitian operators that are localized on different positions l and m, respectively, OTOC [1] is given as

$$C^{l,m}(n) = -\frac{1}{2}\text{Tr}\{[\hat{W}^l(n), \hat{V}^m]^2\}, \tag{A1}$$

which is a measure of the noncommutativity of two operators, $\hat{W}^l$ and $\hat{V}^m$. These are infinite-temperature quantities and involve the entire spectrum of 2^N states. One can use the trick for evaluating OTOC by employing Haar random states of 2^N dimensions $|\Psi_R\rangle$ and calculate the expectation value over $|\Psi_R\rangle$. OTOC is

$$C^{l,m}(n) = -2^{N-1}\langle\Psi_R|[\hat{W}^l(n), \hat{V}^m]^2|\Psi_R\rangle \tag{A2}$$

since the behavior of OTOC is similar for both random states and special initial states ($|\phi\rangle$ and $|\psi\rangle$, respectively). So we consider special initial states, and OTOC is

$$C^{l,m}(n) = -2^{N-1}\langle\psi/\phi|[\hat{W}^l(n), \hat{V}^m]^2|\psi/\phi\rangle. \tag{A3}$$

Figure 7 shows the behavior of TMOTOC in the nonintegrable $\hat{\mathcal{U}}_x$ system using the random initial state ψ_R drawn from the Harr measure. Characteristic time is independent of the Floquet period [Fig. 7(a)], and it depends on the separation between the
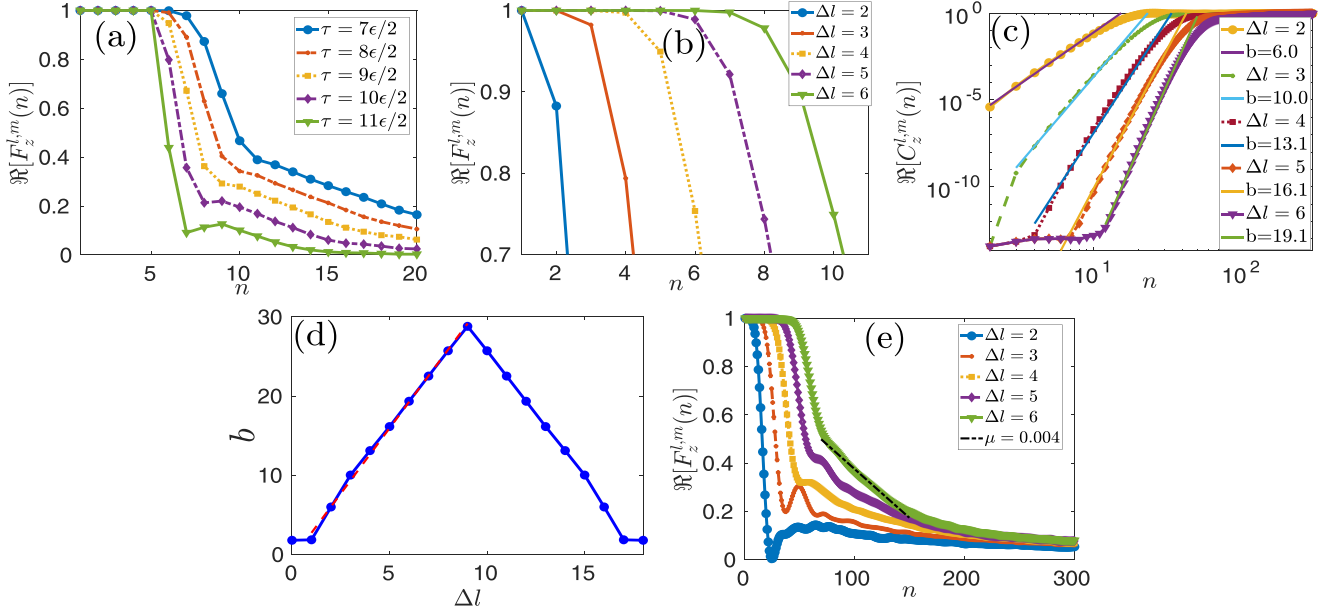
FIG. 7. Nonintegrable closed-chain transverse Ising Floquet system with $J_x = 1$, $h_z = 1$, and $h_x = 1$ of size $N = 18$. (a) Behavior of TMOTOC with the number of kicks n while increasing the Floquet period from $\frac{7\epsilon}{2}$ to $\frac{11\epsilon}{2}$ (right to left), differing by $\frac{\epsilon}{2}$, with fixed $\Delta l = 6$ ($\epsilon = \frac{\pi}{28}$). (b) Initial region of $F_z^{l,m}$ with the number of kicks and increasing Δl (left to right) at fixed Floquet period $\tau = 6\epsilon/2$. (c) $C_z^{l,m}$ with the number of kicks (log-log) with increasing Δl (left to right) at fixed $\tau = \frac{\epsilon}{2}$. (d) Change in the exponent of the power law with Δl. (e) Saturation of $F_z^{l,m}$ with the number of kicks with increasing Δl (left to right).

observables. The number of kicks required to deviate from unity is equal to the separation between the observables [Fig. 7(b)]. The dynamic region of TMOTOC for the nonintegrable shows a power law [Fig. 7(c)] that is similar to Fig. 4(c). The exponent of the power law b depends on Δl [Fig. 7(d)], and its behavior is similar to Fig. 4(d). Saturation of $\Re[F_z^{l,m}(n)]$ follows a linear decaying behavior with a very small slope (0.004) for all Δl [Fig. 7(e)]. There is a very small oscillation in comparison to Fig. 4(e).

APPENDIX B: TIME EVOLUTION OF TMOTOC

The Heisenberg evolution of an operator $\hat{W}(t)$ can be expanded using the Hausdorff-Baker-Campbell (HBC) formula as

$$\hat{W}(t) = \sum_{p=0}^{\infty} \frac{(it)^p}{p!} [\hat{H}, [\hat{H}, \cdots^{\text{p times}}, [\hat{H}, \hat{W}]]]. \tag{B1}$$

If $\hat{W} = \hat{\sigma}_l^{z/x}$, the HBC formula captures the spread of the operator over the spin sites and how it becomes more complex as time increases. Furthermore, direct insertion of Eq. (B1) into Eq. (6) highlights the fact that the short-time growth is characterized by the smallest p where

$$\left[\hat{H}, [\hat{H}, \cdots^{\text{p times}}, [\hat{H}, \hat{\sigma}_l^{x/z}]], \hat{\sigma}_m^{x/z}\right] \neq 0 \tag{B2}$$

due to the time factor t^n that weights the terms in the expansion. We remark that this mechanism points out that the short-time growth is characterized by a general Hamiltonian structure of the system and not by the regular to chaotic regimes observed in the studied spin chains.

We consider the Pauli operator in the transverse direction of the coupling and $\hat{\mathcal{U}}_x = \hat{U}_{xx}\hat{U}_z$, where $\hat{U}_{xx} = \exp[-i\tau(J_x\hat{H}_{xx} + h_x\hat{H}_x)]$ and $\hat{U}_z = \exp(-i\tau h_z\hat{H}_z)$. Using Eq. (B1), the Heisenberg evolution of the spin operator $\hat{\sigma}_z^l$ is obtained:

$$\hat{\sigma}_z^l(n) = (\hat{U}_z^\dagger \hat{U}_{xx}^\dagger)^n \hat{\sigma}_z^l (\hat{U}_{xx}\hat{U}_z)^n; \tag{B3}$$

after the first kick is applied, $\hat{\sigma}_z^l(1)$ is

$$\hat{\sigma}_z^l(1) = \hat{U}_z^\dagger \hat{U}_{xx}^\dagger \hat{\sigma}_z^l \hat{U}_{xx}\hat{U}_z$$

$$= \hat{U}_z^\dagger (\hat{\sigma}_z^l + i\tau[\hat{H}_{xx} + \hat{H}_x, \hat{\sigma}_z^l] + \frac{(i\tau)^2}{2!}[\hat{H}_{xx} + \hat{H}_x, [\hat{H}_{xx} + \hat{H}_x, \hat{\sigma}_z^l]] + \cdots)\hat{U}_z$$

$$= \hat{\sigma}_z^l + i\tau\{\hat{U}_z^\dagger[-2i(\hat{\sigma}_x^{l-1}\hat{\sigma}_y^l + \hat{\sigma}_y^l\hat{\sigma}_x^{l+1} + \hat{\sigma}_y^l)]\hat{U}_z\} + \cdots$$

$$= \hat{\sigma}_z^l + 2\tau\big[\hat{U}_z^\dagger\big(\hat{\sigma}_x^{l-1}\hat{\sigma}_y^l + \hat{\sigma}_y^l\hat{\sigma}_x^{l+1} + \hat{\sigma}_y^l\big)\hat{U}_z\big] + \cdots$$

$$= \hat{\sigma}_z^l + 2\tau\Big\{\hat{\sigma}_x^{l-1}\hat{\sigma}_y^l + \hat{\sigma}_y^l\hat{\sigma}_x^{l+1} + \hat{\sigma}_y^l + i\tau\big(-2i\big[\hat{\sigma}_x^{l-1}\hat{\sigma}_x^l + \hat{\sigma}_y^{l-1}\hat{\sigma}_y^l + \hat{\sigma}_x^l\hat{\sigma}_x^{l+1} + \hat{\sigma}_y^l\hat{\sigma}_y^{l+1} + \hat{\sigma}_x^l\big]\big) + \cdots\Big\} + \cdots$$

$$= \hat{\sigma}_z^l + \big[2\tau\big(\hat{\sigma}_x^{l-1}\hat{\sigma}_y^l + \hat{\sigma}_y^l\hat{\sigma}_x^{l+1} + \hat{\sigma}_y^l\big) + (2\tau)^2\big(\hat{\sigma}_x^{l-1}\hat{\sigma}_x^l + \hat{\sigma}_y^{l-1}\hat{\sigma}_y^l + \hat{\sigma}_x^l\hat{\sigma}_x^{l+1} + \hat{\sigma}_y^l\hat{\sigma}_y^{l+1} + \hat{\sigma}_x^l\big) + \cdots\big] + \cdots. \quad \text{(B4)}$$

We apply the second kick; then $\hat{\sigma}_z^l(2)$ is

$$\hat{\sigma}_z^l(2) = \hat{U}_z^\dagger\hat{U}_{xx}^\dagger\big\{\hat{\sigma}_z^l + \big[2\tau\big(\hat{\sigma}_x^{l-1}\hat{\sigma}_y^l + \hat{\sigma}_y^l\hat{\sigma}_x^{l+1} + \hat{\sigma}_y^l\big) + (2\tau)^2\big(\hat{\sigma}_x^{l-1}\hat{\sigma}_x^l + \hat{\sigma}_y^{l-1}\hat{\sigma}_y^l + \hat{\sigma}_x^l\hat{\sigma}_x^{l+1} + \hat{\sigma}_y^l\hat{\sigma}_y^{l+1} + \hat{\sigma}_x^l\big) + \cdots\big] + \cdots\big\}\hat{U}_{xx}\hat{U}_z$$

$$= \hat{\sigma}_z^l + \big\{4\tau\big(\hat{\sigma}_y^{l-1}\hat{\sigma}_x^l + \hat{\sigma}_y^l\hat{\sigma}_x^{l+1} + \hat{\sigma}_y^l\big) + (2\tau)^2\big(\hat{\sigma}_x^{l-1}\hat{\sigma}_x^l + \hat{\sigma}_y^{l-1}\hat{\sigma}_y^l + \hat{\sigma}_x^l\hat{\sigma}_x^{l+1} + \hat{\sigma}_y^l\hat{\sigma}_y^{l+1} + \hat{\sigma}_x^l\big)$$

$$+ (2\tau)^2\big[\hat{U}_z^\dagger\hat{U}_{xx}^\dagger\big(\hat{\sigma}_y^{l-1}\hat{\sigma}_y^l + \hat{\sigma}_y^l\hat{\sigma}_y^{l+1}\big)\hat{U}_{xx}^\dagger\hat{U}_z^\dagger\big] + \cdots\big\} + \cdots. \quad \text{(B5)}$$

From the above equation, we extract the coefficient of τ^2 which contains the $\hat{\sigma}_y^{l+2}$ term. It is given as

$$(2\tau)^2\big[\hat{U}_z^\dagger\hat{U}_{xx}^\dagger\big(\hat{\sigma}_y^{l-1}\hat{\sigma}_y^l + \hat{\sigma}_y^l\hat{\sigma}_y^{l+1}\big)\hat{U}_{xx}^\dagger\hat{U}_z^\dagger\big] = (2\tau)^2\hat{U}_z^\dagger\big(\hat{\sigma}_y^l\hat{\sigma}_y^{l+1} + i\tau[\hat{H}_{xx} + \hat{H}_x, \hat{\sigma}_y^l\hat{\sigma}_y^{l+1}] + \cdots\big)\hat{U}_z \quad \text{(B6)}$$

$$= (2\tau)^2\big(\cdots - 2\tau\hat{\sigma}_y^{l-1}\hat{\sigma}_z^l\hat{\sigma}_y^{l+1} - 2\tau\hat{\sigma}_y^l\hat{\sigma}_z^{l+1}\hat{\sigma}_y^{l+2} + \cdots\big).$$

For $m = l + 2$, $C_z^{l,m}(2) = 64\tau^6$. We apply the third kick, and then $\hat{\sigma}_z^l(3)$ is

$$\hat{\sigma}_z^l(3) = \hat{U}_z^\dagger\hat{U}_{xx}^\dagger\big\{\hat{\sigma}_z^l + \big[4\tau\big(\hat{\sigma}_y^{l-1}\hat{\sigma}_x^l + \hat{\sigma}_y^l\hat{\sigma}_x^{l+1} + \hat{\sigma}_y^l\big) + (2\tau)^2\big(\hat{\sigma}_x^{l-1}\hat{\sigma}_x^l + \hat{\sigma}_y^{l-1}\hat{\sigma}_y^l + \hat{\sigma}_x^l\hat{\sigma}_x^{l+1} + \hat{\sigma}_y^l\hat{\sigma}_y^{l+1} + \hat{\sigma}_x^l\big) + \cdots\big] + \cdots\big\}\hat{U}_{xx}\hat{U}_z$$

$$= \big\{\hat{\sigma}_z^l + \big[6\tau\big(\hat{\sigma}_y^{l-1}\hat{\sigma}_x^l + \hat{\sigma}_y^l\hat{\sigma}_x^{l+1} + \hat{\sigma}_y^l\big) + (2\tau)^2\big(\hat{\sigma}_x^{l-1}\hat{\sigma}_x^l + \hat{\sigma}_y^{l-1}\hat{\sigma}_y^l + \hat{\sigma}_x^l\hat{\sigma}_x^{l+1} + \hat{\sigma}_y^l\hat{\sigma}_y^{l+1} + \hat{\sigma}_x^l\big) + \cdots\big] + \cdots\big\}.$$

For $\Delta l = 1$, $m = l + 1$, the dominating exponent of the power law of OTOC is

$$C_z^{l,l+1}(1) = 4\tau^2\langle\phi_0|\big[\big(\hat{\sigma}_y^l\hat{\sigma}_x^{l+1} + \hat{\sigma}_y^l\big), \hat{\sigma}_z^m\big]^2|\phi_0\rangle \quad \text{(B7)}$$

$$= 4\langle\phi_0|\big(-i\hat{\sigma}_y^l\hat{\sigma}_y^{l+1}\big)^2|\phi_0\rangle = 4\tau^2.$$

Similarly, $C_z^{l,l+1}(2) = 16\tau^2$, and $C_z^{l,l+1}(3) = 36\tau^2$.

The dominating exponent of the power law of OTOC is $C_z^{l,l+2}(1) = 0$, $C_z^{l,l+2}(2) = 64\tau^6$. This power-law growth approximately matches the dynamic region of the Eq. (17).

APPENDIX C: TIME EVOLUTION OF LMOTOC

We consider the Pauli operator in the longitudinal direction of the coupling. Using Eq. (B1), the Heisenberg evolution of the spin operator $\hat{\sigma}_x^l$ is obtained:

$$\hat{\sigma}_x^l(n) = (\hat{U}_z^\dagger\hat{U}_{xx}^\dagger)^n\hat{\sigma}_x^l(\hat{U}_{xx}\hat{U}_z)^n;$$

after the first kick is applied, $\hat{\sigma}_x^l(1)$ is

$$\hat{\sigma}_x^l(1) = \hat{U}_z^\dagger\hat{U}_{xx}^\dagger\hat{\sigma}_x^l\hat{U}_{xx}\hat{U}_z$$

$$= \hat{U}_z^\dagger\Big(\hat{\sigma}_x^l + i\tau\big[\hat{H}_{xx} + \hat{H}_x, \hat{\sigma}_x^l\big] + \frac{(i\tau)^2}{2!}[\hat{H}_{xx} + \hat{H}_x, [\hat{H}_{xx} + \hat{H}_x, \hat{\sigma}_x^l]] + \cdots\Big)\hat{U}_z.$$

Since $[\hat{H}_{xx} + \hat{H}_x, \hat{\sigma}_x^l] = 0$, then

$$\hat{\sigma}_x^l(1) = \hat{U}_z^\dagger\hat{\sigma}_x^l\hat{U}_z$$

$$= \hat{\sigma}_x^l + i\tau\big[\hat{H}_z, \hat{\sigma}_x^l\big] + \frac{(i\tau)^2}{2!}[\hat{H}_z, [\hat{H}_z, \hat{\sigma}_x^l]] + \cdots = \hat{\sigma}_x^l(1) = \hat{\sigma}_x^l - 2\tau\hat{\sigma}_y^l + \cdots. \quad \text{(C1)}$$

We apply the second kick; then $\hat{\sigma}_x^l(2)$ is

$$\hat{\sigma}_x^l(2) = \hat{U}_z^\dagger\hat{U}_{xx}^\dagger\hat{\sigma}_x^l(1)\hat{U}_{xx}\hat{U}_z$$

$$= U_z^\dagger\hat{U}_{xx}^\dagger\big(\hat{\sigma}_x^l - 2\tau\hat{\sigma}_y^l + \cdots\big)\hat{U}_{xx}\hat{U}_z$$

$$= \big(U_z^\dagger\hat{U}_{xx}^\dagger\hat{\sigma}_x^l\hat{U}_{xx}\hat{U}_z - 2\tau U_z^\dagger\hat{U}_{xx}^\dagger\hat{\sigma}_y^l\hat{U}_{xx}\hat{U}_z + \cdots\big)$$

$$= \big\{\hat{\sigma}_x^l - 2\tau\hat{\sigma}_y^l - 2\tau U_z^\dagger\big[\hat{\sigma}_y^l - 2\tau\big(\hat{\sigma}_x^{l-1}\hat{\sigma}_z^l + \hat{\sigma}_z^l\hat{\sigma}_y^{l+1} + \hat{\sigma}_z^l\big) + \cdots\big]\hat{U}_z + \cdots\big\}$$

$$= \big(\hat{\sigma}_x^l - 2\tau\hat{\sigma}_y^l - 2\tau\{\hat{\sigma}_y^l - 2\tau\hat{\sigma}_y^{l-1}\hat{\sigma}_z^l - 2\tau\hat{\sigma}_z^l\hat{\sigma}_y^{l+1} - 2\tau\hat{\sigma}_z^l + i\tau\big[-2i\hat{\sigma}_x^l - 2\tau(-2i)\hat{\sigma}_z^l\hat{\sigma}_y^{l+1}\big] + \cdots\} + \cdots\big)$$

$$= \big[\hat{\sigma}_x^l - 4\tau\hat{\sigma}_y^l + (2\tau)^2\big(\hat{\sigma}_z^l\hat{\sigma}_y^{l+1} + \hat{\sigma}_x^l + \hat{\sigma}_z^l\big) + (2\tau)^3\hat{\sigma}_z^l\hat{\sigma}_y^{l+1} + \cdots\big]. \quad \text{(C2)}$$

We apply the third kick; then $\hat{\sigma}_x^l(3)$ is

$$\hat{\sigma}_x^l(3) = \hat{U}_z^\dagger \hat{U}_{xx}^\dagger [\hat{\sigma}_x^l - 4\tau \hat{\sigma}_y^l + (2\tau)^2(\hat{\sigma}_z^l \hat{\sigma}_y^{l+1} + \hat{\sigma}_x^l + \hat{\sigma}_z^l) + (2\tau)^3 \hat{\sigma}_z^l \hat{\sigma}_y^{l+1} + \cdots] \hat{U}_{xx} \hat{U}_z$$

$$= [\hat{\sigma}_x^l - 6\tau \hat{\sigma}_y^l + 2(2\tau)^2(\hat{\sigma}_z^l \hat{\sigma}_y^{l+1} + \hat{\sigma}_x^l + \hat{\sigma}_z^l) + 2(2\tau)^3 \hat{\sigma}_z^l \hat{\sigma}_y^{l+1} + \cdots] + \cdots . \tag{C3}$$

Consider $\Delta l = 1$, $m = l + 1 C_x^{l,l+1}(1) = 0$, $C_x^{l,l+1}(2) = 64\tau^6$, and $C_x^{l,l+1}(3) = 256\tau^6$. The exponent of the power law approximately matches Eq. (19).

---

[1] A. I. Larkin and Y. N. Ovchinnikov, Sov. Phys. JETP **28**, 1200 (1969).

[2] A. Singh, K. Sachan, L. Chotorlishvili, V. Vipin, and S. K. Mishra, Eur. Phys. J. D **76**, 17 (2022).

[3] S. H. Shenker and D. Stanford, J. High Energy Phys. 05 (2015) 132.

[4] M. C. Gutzwiller, *Chaos in Classical and Quantum Mechanics* (Springer, New York, 2013), Vol. 1.

[5] F. Haake, Quantum Signatures of Chaos, in *Quantum Coherence in Mesoscopic Systems*, edited by B. Kramer (Springer, Boston, MA, 1991), pp. 583–595.

[6] P. Hosur, X.-L. Qi, D. A. Roberts, and B. Yoshida, J. High Energy Phys. 02 (2016) 004.

[7] E. B. Rozenbaum, S. Ganeshan, and V. Galitski, Phys. Rev. Lett. **118**, 086801 (2017).

[8] I. García-Mata, M. Saraceno, R. A. Jalabert, A. J. Roncaglia, and D. A. Wisniacki, Phys. Rev. Lett. **121**, 210601 (2018).

[9] R. K. Shukla, G. K. Naik, and S. K. Mishra, Europhys. Lett. **132**, 47003 (2020).

[10] E. B. Rozenbaum, L. A. Bunimovich, and V. Galitski, Phys. Rev. Lett. **125**, 014101 (2020).

[11] J. Maldacena, S. H. Shenker, and D. Stanford, J. High Energy Phys. 08 (2016) 106.

[12] D. Stanford, J. High Energy Phys. 10 (2016) 009.

[13] I. L. Aleiner, L. Faoro, and L. B. Ioffe, Ann. Phys. (NY) **375**, 378 (2016).

[14] D. A. Roberts and B. Swingle, Phys. Rev. Lett. **117**, 091602 (2016).

[15] D. A. Roberts, D. Stanford, and L. Susskind, J. High Energy Phys. 03 (2015) 051.

[16] T. Bilitewski, S. Bhattacharjee, and R. Moessner, Phys. Rev. Lett. **121**, 250602 (2018).

[17] A. Das, S. Chakrabarty, A. Dhar, A. Kundu, D. A. Huse, R. Moessner, S. S. Ray, and S. Bhattacharjee, Phys. Rev. Lett. **121**, 024101 (2018).

[18] Y. Huang, Y.-L. Zhang, and X. Chen, Ann. Phys. (Berlin, Ger.) **529**, 1600318 (2017).

[19] K. X. Wei, C. Ramanathan, and P. Cappellaro, Phys. Rev. Lett. **120**, 070501 (2018).

[20] C.-J. Lin and O. I. Motrunich, Phys. Rev. B **97**, 144304 (2018).

[21] N. Abeling, L. Cevolani, and S. Kehrein, Sci. Post Phys. **5**, 052 (2018).

[22] C. B. Dağ, K. Sun, and L.-M. Duan, Phys. Rev. Lett. **123**, 140602 (2019).

[23] S. Grozdanov, K. Schalm, and V. Scopelliti, Phys. Rev. Lett. **120**, 231601 (2018).

[24] M. Heyl, F. Pollmann, and B. Dóra, Phys. Rev. Lett. **121**, 016801 (2018).

[25] B. Chen, X. Hou, F. Zhou, P. Qian, H. Shen, and N. Xu, Appl. Phys. Lett. **116**, 194002 (2020).

[26] N. Y. Yao, F. Grusdt, B. Swingle, M. D. Lukin, D. M. Stamper-Kurn, J. E. Moore, and E. A. Demler, arXiv:1607.01801.

[27] B. Swingle, G. Bentsen, M. Schleier-Smith, and P. Hayden, Phys. Rev. A **94**, 040302(R) (2016).

[28] G. Zhu, M. Hafezi, and T. Grover, Phys. Rev. A **94**, 062329 (2016).

[29] M. Campisi and J. Goold, Phys. Rev. E **95**, 062127 (2017).

[30] N. Yunger Halpern, Phys. Rev. A **95**, 012120 (2017).

[31] J. Li, R. Fan, H. Wang, B. Ye, B. Zeng, H. Zhai, X. Peng, and J. Du, Phys. Rev. X **7**, 031011 (2017).

[32] K. A. Landsman, C. Figgatt, T. Schuster, N. M. Linke, B. Yoshida, N. Y. Yao, and C. Monroe, Nature (London) **567**, 61 (2019).

[33] M. K. Joshi, A. Elben, B. Vermersch, T. Brydges, C. Maier, P. Zoller, R. Blatt, and C. F. Roos, Phys. Rev. Lett. **124**, 240505 (2020).

[34] E. J. Meier, J. Ang'ong'a, F. A. An, and B. Gadway, Phys. Rev. A **100**, 013623 (2019).

[35] Y. Gu and X.-L. Qi, J. High Energy Phys. 08 (2016) 129.

[36] V. Oganesyan and D. A. Huse, Phys. Rev. B **75**, 155111 (2007).

[37] E. Altman and R. Vosk, Annu. Rev. Condens. Matter Phys. **6**, 383 (2015).

[38] R. Nandkishore and D. A. Huse, Annu. Rev. Condens. Matter Phys. **6**, 15 (2015).

[39] P. W. Anderson, Phys. Rev. **109**, 1492 (1958).

[40] S. Xu and B. Swingle, Nat. Phys. **16**, 199 (2020).

[41] S. Xu and B. Swingle, Phys. Rev. X **9**, 031048 (2019).

[42] I. Kukuljan, S. Grozdanov, and T. Prosen, Phys. Rev. B **96**, 060301(R) (2017).

[43] E. M. Fortes, I. García-Mata, R. A. Jalabert, and D. A. Wisniacki, Phys. Rev. E **100**, 042201 (2019).

[44] B. Craps, M. De Clerck, D. Janssens, V. Luyten, and C. Rabideau, Phys. Rev. B **101**, 174313 (2020).

[45] N. Roy and A. Sharma, J. Phys.: Condens. Matter **33**, 334001 (2021).

[46] H. Yan, J.-Z. Wang, and W.-G. Wang, Commun. Theor. Phys. **71**, 1359 (2019).

[47] J.-H. Bao and C.-Y. Zhang, Commun. Theor. Phys. **72**, 085103 (2020).

[48] B. Dóra and R. Moessner, Phys. Rev. Lett. **119**, 026802 (2017).

[49] J. Riddell and E. S. Sørensen, Phys. Rev. B **99**, 054205 (2019).

[50] J. Lee, D. Kim, and D.-H. Kim, Phys. Rev. B **99**, 184202 (2019).

[51] G. Casati, B. Chirikov, F. Izrailev, and J. Ford, *Lecture Notes in Physics* (Springer, Berlin, 1979), Vol. 93, pp. 334.

[52] B. V. Chirikov, Research Concerning the Theory of Non-linear Resonance and Stochasticity, Preprint No. 267 (Institute of Nuclear Physics, Novosibirsk, 1969).

[53] P. L. Kapitza, Sov. Phys. JETP **21**, 588 (1951).

[54] S. Rahav, I. Gilary, and S. Fishman, Phys. Rev. A **68**, 013820 (2003).

[55] S. Rahav, I. Gilary, and S. Fishman, Phys. Rev. Lett. **91**, 110404 (2003).

[56] L. Landau and E. Lifshitz, *Course of Theoretical Physics* (Elsevier, Moscow, 1987), Vol. 6.

[57] J. Zhang, P. W. Hess, A. Kyprianidis, P. Becker, A. Lee, J. Smith, G. Pagano, I.-D. Potirniche, A. C. Potter, A. Vishwanath, N. Y. Yao, and C. Monroe, Nature (London) **543**, 217 (2017).

[58] A. Russomanno, F. Iemini, M. Dalmonte, and R. Fazio, Phys. Rev. B **95**, 214307 (2017).

[59] K. Wintersperger, C. Braun, F. N. Ünal, A. Eckardt, M. Di Liberto, N. Goldman, I. Bloch, and M. Aidelsburger, Nat. Phys. **16**, 1058 (2020).

[60] W. Zhu, Y. D. Chong, and J. Gong, Phys. Rev. B **104**, L020302 (2021).

[61] N. Goldman and J. Dalibard, Phys. Rev. X **4**, 031027 (2014).

[62] H. Ammann, R. Gray, I. Shvarchuck, and N. Christensen, Phys. Rev. Lett. **80**, 4111 (1998).

[63] M. B. d'Arcy, R. M. Godun, M. K. Oberthaler, D. Cassettari, and G. S. Summy, Phys. Rev. Lett. **87**, 074102 (2001).

[64] L. D'Alessio and A. Polkovnikov, Ann. Phys. (NY) **333**, 19 (2013).

[65] V. Gritsev and A. Polkovnikov, Sci. Post Phys. **2**, 021 (2017).

[66] A. Lakshminarayan and V. Subrahmanyam, Phys. Rev. A **71**, 062334 (2005).

[67] L. D'Alessio and M. Rigol, Phys. Rev. X **4**, 041048 (2014).

[68] G. K. Naik, R. Singh, and S. K. Mishra, Phys. Rev. A **99**, 032321 (2019).

[69] S. K. Mishra, A. Lakshminarayan, and V. Subrahmanyam, Phys. Rev. A **91**, 022318 (2015).

[70] S. K. Mishra and A. Lakshminarayan, Europhys. Lett. **105**, 10002 (2014).

[71] D. Rossini, S. Suzuki, G. Mussardo, G. E. Santoro, and A. Silva, Phys. Rev. B **82**, 144302 (2010).

[72] F. H. Essler and M. Fagotti, J. Stat. Mech. (2016) 064002.

[73] A. Russomanno, A. Silva, and G. E. Santoro, Phys. Rev. Lett. **109**, 257201 (2012).

[74] A. Russomanno, A. Silva, and G. E. Santoro, J. Stat. Mech. (2013) P09012.

[75] Z. Ovadyahu, Phys. Rev. Lett. **108**, 156602 (2012).

[76] S. Iwai, M. Ono, A. Maeda, H. Matsuzaki, H. Kishida, H. Okamoto, and Y. Tokura, Phys. Rev. Lett. **91**, 057401 (2003).

[77] S. Kaiser, C. R. Hunt, D. Nicoletti, W. Hu, I. Gierz, H. Y. Liu, M. Le Tacon, T. Loew, D. Haug, B. Keimer, and A. Cavalleri, Phys. Rev. B **89**, 184516 (2014).

[78] S. Zamani, R. Jafari, and A. Langari, Phys. Rev. B **105**, 094304 (2022).

[79] T. Prosen, Prog. Theor. Phys. Suppl. **139**, 191 (2000).

[80] T. C. V. Prosen, Phys. Rev. E **65**, 036208 (2002).

[81] S. Sachdev, *Quantum Phase Transitions*, 2nd ed. (Cambridge University Press, Cambridge, 2011).

[82] M. Gärttner, J. G. Bohnet, A. Safavi-Naini, M. L. Wall, J. J. Bollinger, and A. M. Rey, Nat. Phys. **13**, 781 (2017).